

Controllable Water Vapor Assisted Chemical Vapor Transport Synthesis of WS₂-MoS₂ Heterostructure

*Yuzhou Zhao and Song Jin**

Department of Chemistry, University of Wisconsin – Madison, 1101 University Avenue,
Madison, Wisconsin 53706, United States

*Corresponding authors. E-mail: jin@chem.wisc.edu

Keywords: transition metal dichalcogenides, heterostructures, water vapor, chemical vapor transport

Abstract: The vapor phase synthesis of two-dimensional transition-metal dichalcogenides (MX₂) and their heterostructures is often poorly reproducible and sensitive to uncontrolled environmental humidity. It was recently realized that water vapor can play important roles in the growth of MX₂ by reacting with MX₂ at high temperature to form volatile metal oxyhydroxide (MO_x(OH)_y) and hydrogen chalcogenides (H₂X) that dramatically change the growth processes. Here we report the controllable synthesis of WS₂, MoS₂, and their heterostructures using water-assisted chemical vapor transport (CVT). The water vapor can be tunably delivered by thermal dehydration of calcium sulfate dihydrate (CaSO₄·2H₂O) solid precursor, which not only provides much lower vapor pressure baseline and a wider tunable range than liquid water, but also can be readily integrated into a chemical vapor deposition process. This allows controlled growth of monolayer,

multilayers, and spiral nanoplates of WS₂, as well as the lateral epitaxial growth on the edge of MX₂, and more reproducible growth of large area WS₂-MoS₂ heterostructures. Raman and photoluminescence spectral mappings confirm the various types of WS₂-MoS₂ heterostructures. These results reveal insights into the growth mechanisms of MX₂ and provide a general approach to the controllable growth of other metal chalcogenides.

Two-dimensional (2D) transition metal dichalcogenides (TMDs, generally expressed as MX_2 , $\text{M} = \text{Mo}, \text{W}, \text{etc.}$; $\text{X} = \text{S}, \text{Se}, \text{Te}$) and their heterostructures have attracted increasing research interests in recent years due to abundant choice of materials,¹⁻³ their fascinating electro-optical properties,^{1, 4-8} and potential applications in high-performance and flexible optoelectronic devices.^{1,4-8} While mechanical exfoliation of high-quality single crystals⁹⁻¹¹ is commonly used for fundamental studies and liquid exfoliation¹²⁻¹³ has been demonstrated for mass production, vapor phase growth provides scalable approaches to grow high-quality and large-area 2D single crystals with atomic layer thickness.^{3, 14-18} The conventional vapor phase growth methods for MX_2 can be categorized by the precursors used in reactions, such as metal oxides,¹⁶⁻²⁷ metal chlorides,²⁸⁻³⁰ metal-organic precursors,³¹⁻³⁴ as well as metal dichalcogenides.^{20, 35-41} Chemical vapor deposition (CVD) synthesis of MX_2 ^{15, 42} have been commonly used to successfully enable diverse morphologies, such as monolayers,^{16-18, 25-26} monolayer polycrystalline thin films,^{33-34, 43-44} spiral nanoplates,^{39-40, 45-48} and lateral^{19-22, 35-37} and vertical^{21-22, 28-29} heterostructures, *etc.*

Despite these successes, the vapor growth of 2D MX_2 layers and their heterostructures are notoriously difficult to reproduce. Water vapor as a common but fluctuating atmospheric constituent could be one of the many causes of the irreproducibility in vapor phase growth of MX_2 . It is believed that most of the precursors used for MX_2 synthesis are also sensitive to water vapor and environmental humidity during the reaction, where the presence of water reacts with the precursors causing hydrolysis or oxidations.^{28,35,49} Uncontrolled moisture could be the reason that causes MX_2 vapor phase growth less reliable and reproducible. So researchers are always trying to minimize the effect of moisture, often by keeping the reactor under vacuum for long time or baking the reactor before reactions. Although the importance of minimizing moisture is commonly accepted in the community, the role water plays in the reactions is less studied. It was only until

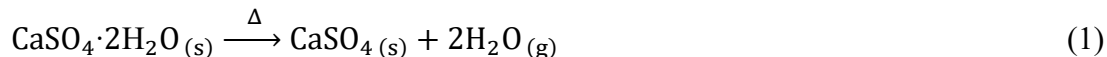
recently that the moisture level was carefully monitored during synthesis or water vapor was intentionally used in the growth of MX_2 and their heterostructures.^{28, 35, 49} For example, the correlation between the ambient humidity and the effective partial pressure of the MoCl_5 precursor during the reaction was reported, and layer-controlled MoS_2 vertical heterostructure can be synthesized by carefully tracking the humidity and compensating its effect with reduction in the reaction time or precursor temperature.²⁸ Furthermore, it was reported that water vapor can react with MX_2 at high temperature to form volatile metal oxyhydroxide $[\text{MO}_x(\text{OH})_y]$ species and hydrogen chalcogenides (H_2X) that dramatically change the growth mechanisms and increase the effective vapor pressure of the growth precursors.³⁵ By utilizing water vapor generated from a water bubbler and hydrogen gas controlled by mass flow controller, exquisite multijunctions of lateral heterostructures were recently realized.³⁵ Interestingly, water vapor has also been previously identified as a crucial parameter in the CVD synthesis of single-walled carbon nanotube,⁵⁰⁻⁵² graphene,⁵³ and hexagonal boron nitride,⁵⁴ where it reacts as a gentle oxidizer and etching reagent.

On the other hand, many recent studies report physical vapor deposition (PVD) of MX_2 using MX_2 powder as the precursor in ambient pressure CVD setups.^{20, 36-41} However, considering the high melting points of MX_2 (MoS_2 : 2380 °C; WS_2 : 1800 °C),⁵⁵ and the high melting temperatures of the corresponding metal element (Mo: 2623 °C; W: 3422 °C), the reported reaction temperatures seem rather low for a PVD mechanism in ambient pressure. In fact, the thermal stability of MX_2 in ambient or vacuum has been controversial.⁵⁵⁻⁵⁶ It is possible that such confusing thermal stability could be caused by the trace water vapor present in those experiments. This also suggests that some growth reactions that were believed to be simple thermal PVD could actually go through a chemical vapor transport (CVT) pathway with water vapor actually serving as the transport

regent.^{20, 36-41} Such water-assisted CVT hypothesis also suggests the importance of not only minimizing the water vapor before or during reactions but also controlling water vapor intentionally to control the synthesis and improve the reproducibility.

In this work, we report the controllable synthesis of WS₂ monolayers, few layers, and spiral nanoplates, as well as various types of WS₂-MoS₂ heterostructures using water-assisted chemical vapor transport. We utilize the thermal dehydration of solid water vapor source calcium sulfate dihydrate (CaSO₄·2H₂O) to conveniently control the amount of water vapor. This facile approach not only provides much lower vapor pressure baseline and a wider tunable range than liquid water precursor, but also can be easily integrated into a CVD process without further modifying the setup. This allows the precise control of the growth of various WS₂ (and other MX₂) monolayer and nanostructures, the lateral epitaxial growth of MoS₂ on the edge of WS₂, and more reproducible growth of 3 different types of large-area heterostructures of WS₂-MoS₂. Raman and photoluminescence (PL) mappings confirm the different types of heterostructures. Our research provides chemical insights into the growth mechanism of MX₂ materials and it can potentially be a general approach to controllable grow other MX₂ materials.

We generate water vapor from CaSO₄·2H₂O solid, also known as gypsum in its mineral form. When gypsum is heated, the water of hydration is released to produce CaSO₄, as shown below (the partially dehydrated gypsum is also known as plaster of Paris):



The anhydrous CaSO₄ is powerful in absorbing water at room temperature thus can be effectively used as a common desiccant commercially known as “Drierite”. Conversely, it is difficult to dehydrate CaSO₄·2H₂O at room temperature, however, when CaSO₄·2H₂O is heated, it

can be used to generate water vapor with different rates at different temperatures. Here we first examined the ability of $\text{CaSO}_4 \cdot 2\text{H}_2\text{O}$ to release water vapor at different temperature. Figure 1a shows the percent mass change when 10 mg $\text{CaSO}_4 \cdot 2\text{H}_2\text{O}$ was heated and monitored as a function of time at different isothermal temperatures under constant N_2 flow of 100 sccm in a thermogravimetric (TGA) instrument. Relatively constant dehydration rate can be observed at each temperature from 80 to 120 °C, which shows that heated $\text{CaSO}_4 \cdot 2\text{H}_2\text{O}$ can serve as a stable water source during the reaction. The weight percent stabilized at 79.1%, consistent with a final dehydrated product of CaSO_4 as shown in the Equation 1.

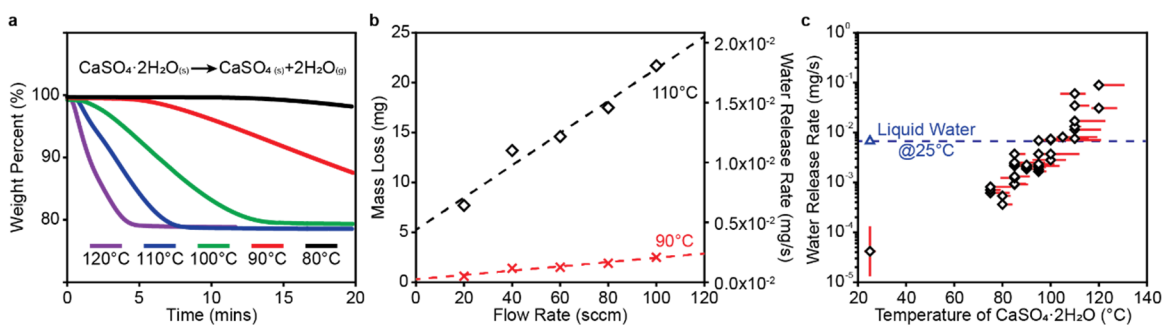
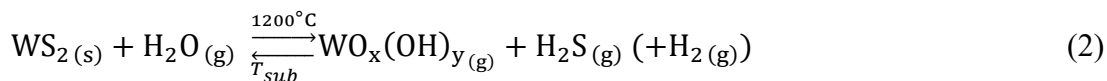


Figure 1. (a) Thermal decomposition of 10 mg $\text{CaSO}_4 \cdot 2\text{H}_2\text{O}$ at isothermal conditions as a function of time at different temperatures, showing definite water vapor release rate at different temperature, to eventually 79.1 wt% corresponding to the complete loss of water. (b) The experimental water vapor release rates of $\text{CaSO}_4 \cdot 2\text{H}_2\text{O}$ at different temperatures shows a linear dependence on the flow rate of carrier gas. The rate was measured by measuring the mass loss of $\sim 1\text{g}$ $\text{CaSO}_4 \cdot 2\text{H}_2\text{O}$ before and after being held at a fixed temperature for 20 mins. (c) The relationship between the experimental water vapor release rate and the temperature of $\text{CaSO}_4 \cdot 2\text{H}_2\text{O}$, showing a wide dynamic range of controlled water vapor supply. All data points were measured with 100 sccm Ar flow and $\sim 1\text{g}$ initial mass of $\text{CaSO}_4 \cdot 2\text{H}_2\text{O}$. The horizontal error bars represent the range of the highest temperature measured before temperature was stabilized

and the lowest temperature during the reaction. The blue horizontal dash line represents the experimental water vapor release rate when liquid water in an alumina boat at 25 °C is used as the water source.

Although in a CVD system the decomposition rate could not be directly monitored *in operando*, the experimental water vapor release rate could be determined by measuring the mass change of $\text{CaSO}_4 \cdot 2\text{H}_2\text{O}$ before and after reaction, as well as the time at the chosen elevated temperature. In a typical reaction where the temperature of $\text{CaSO}_4 \cdot 2\text{H}_2\text{O}$ was controlled by heating tapes (See Experimental Section), only less than 3% of the total 1g mass of $\text{CaSO}_4 \cdot 2\text{H}_2\text{O}$ would be released during the reaction time, which is much less than the 20.9% weight loss limit. The experimental water vapor release rate also shows a linear dependence on the flow rate of carrier gas at different temperatures (Figure 1b). This suggests that the released water vapor reaches an equilibrium with the $\text{CaSO}_4 \cdot 2\text{H}_2\text{O}$ solid locally in the reactor before being swept away by carrier gas. A wide dynamic range of water vapor release rate can be achieved using $\text{CaSO}_4 \cdot 2\text{H}_2\text{O}$ as the water source. As shown in Figure 1c, at a fixed Ar flow rate of 100 sccm, the experimental water vapor release rate can be tuned from 10^{-4} to 10^{-1} mg/s in the temperature range from 80 to 120 °C, which is equivalent to a flow rate of 10^{-3} to 10^0 sccm of pure water vapor. In comparison, the water vapor release rate of 0.1 mL liquid water placed in an alumina boat was measured to be around 7×10^{-3} mg/s under 100 sccm Ar flow (marked as the blue dashed line in Figure 1c). Although water vapor can also be delivered by using a gas bubbler, it requires a more complicated setup, and has more limited range of release rate, especially at the more critical lower range. In contrast, heating $\text{CaSO}_4 \cdot 2\text{H}_2\text{O}$ solid provides a more controllable delivery of water vapor in a much wider range without using complicated setups.

We can utilize this controllable water vapor delivery to enable the reproducible vapor phase growth of MX_2 . Although the growth method can be generally applied to WS_2 , MoS_2 , WSe_2 , MoSe_2 (Figure S1), we are focusing on optimizing and understanding the growth of WS_2 . In a typical growth reaction of WS_2 (Figure 2a, see Experimental Sections for details), $\text{CaSO}_4 \cdot 2\text{H}_2\text{O}$ was placed at the upstream far away from the three-zone tube furnace. This allows $\text{CaSO}_4 \cdot 2\text{H}_2\text{O}$ to stay at room temperature even when the furnace was heated to a high temperature, making it possible to use heating tapes to precisely control the temperature of $\text{CaSO}_4 \cdot 2\text{H}_2\text{O}$ during the reaction. The WS_2 precursor was placed in the center of Zone 1, and a large piece of 300 nm SiO_2/Si substrate was placed between Zone 2 and Zone 3, under an Argon flow of 100 sccm at 800 torr to minimize the penetration of ambient moisture into the reactor. When $\text{CaSO}_4 \cdot 2\text{H}_2\text{O}$, Zone 2 and Zone 3 were heated up to the desired water precursor temperature (T_w , varied from 80 °C to 120 °C), 1200 °C and 800 °C (See a representative example of the actual temperature profiles in Figure S2), respectively and stabilized, the WS_2 precursor was pushed into Zone 2 to initiate the reaction. The water vapor released from $\text{CaSO}_4 \cdot 2\text{H}_2\text{O}$ is transported downstream by the carrier gas and reacts with WS_2 precursor at 1200 °C, which form volatile $\text{WO}_x(\text{OH})_y$ gas species and H_2S gas,³⁵ as follows:



These gaseous intermediates are transported downstream and react to form WS_2 on the substrate at lower temperature (Equation 2, the reverse direction). Note the equations are written in a general form because the oxidation states of tungsten might change during the reactions, which lead to the formation of hydrogen. The more specific reaction mechanisms still need further research. Essentially, when water vapor is present, the WS_2 growth reaction does not take place through a physical evaporation of WS_2 as commonly assumed, but rather water serves as the transport

reagent for the chemical vapor transport of WS₂. Such CVT mechanism is supported by the observation of various tungsten oxide species formed on WS₂ precursor and substrate as the side products (Figure S3), particularly at high water vapor release rate conditions:



Although the CVT mechanism would generate WO_x(OH)_y and H₂S stoichiometrically, due to the formation of tungsten oxide, WO_x(OH)_y species in gas phase would be consumed faster than H₂S. As the reaction goes on, the ratio of H₂S and WO_x(OH)_y could increase to slightly larger than the stoichiometric ratio of 2:1 at different positions, which leads to the triangular and truncated triangular shape of MX₂ products, as previously reported.⁵⁷⁻⁵⁸

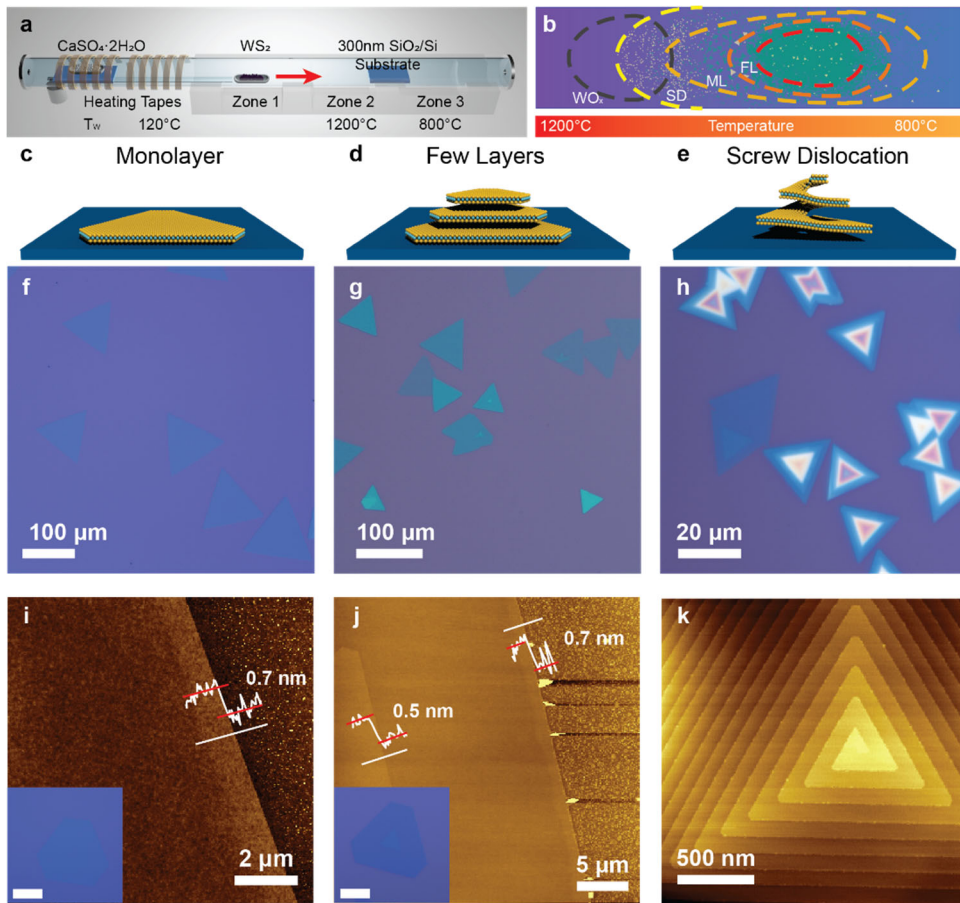


Figure 2. (a) Schematic illustration of the experimental setup of WS₂ growth by water-assisted chemical vapor transport. The WS₂ precursor was pushed into Zone 2 after all temperatures were stable. (b) Schematic illustration of the representative spatial distribution of different WS₂ products on the SiO₂/Si substrate: spiral nanoplates (SD, yellow), monolayer (ML, amber color), and few layers (FL, orange). The region enclosed by black dashed circle is the major growth region of WO_x by product. The schematic structures (c-e), the optical (f-h) and atomic force microscopy images (i-k) of various WS₂ products: (c, f, i) monolayer, (d, g, j) few-layer nanoplate, (e, h, k) nanoplates with screw dislocations. The scale car in insets of (i, j) are 50 μm.

We consistently found different WS₂ products on different regions of the substrate (Figure 2b) when the CaSO₄·2H₂O was heated (i.e. the T_w) between 100 °C and 110 °C. Monolayer (ML, Figure 2c), few layers (FL, Figure 2d), and thick spiral nanoplates grown via a screw dislocation driven mechanisms (SD, Figure 2e) are the three typical and well-defined morphologies of single crystalline structures, as shown in optical microscope images (Figure 2f-h), as well as atomic force microscope (AFM) images and height profiles (Figure 2i-k). The lateral size of monolayer and few layer WS₂ plates are typically around 100 μm, with the thickness of few layer plates varying from 2 to 5 layers. Representative larger area optical images of the various types of products are shown in Figure S4. These morphologies are spatially distributed along the substrate in a predictable sequence. For example, when the CaSO₄·2H₂O was heated to 100 °C, along the gas flow direction from the temperature zone of ~1100 °C to ~900 °C on the substrate, one can find morphologies following a sequence of spiral plates, monolayer WS₂, and few layers WS₂. From ~900 °C to ~800 °C, the reverse sequence happens (Figure 2b). Besides such spatial distribution of morphologies, the more advantageous aspect of this water vapor assisted CVT method is that we now have the

ability to control the morphologies in a specific region of the substrate with controlled delivery of water vapor by changing the heating temperature of $\text{CaSO}_4 \cdot 2\text{H}_2\text{O}$ (T_w). Specifically, by heating $\text{CaSO}_4 \cdot 2\text{H}_2\text{O}$ to $\sim 85^\circ\text{C}$, monolayer and dislocated WS_2 are the dominant morphologies at the temperature zone of around 1000°C on the substrate. Further increasing T_w to 120°C would sequentially yield more few layer growth and polycrystalline growth but less monolayer growth in the same substrate region; while decreasing T_w would sequentially yield more screw dislocation growth when T_w is $\sim 80^\circ\text{C}$. Eventually, when T_w is below 75°C , there was no growth on the substrate (an example is shown in Figure S4a). The typical spatial distributions of various growth products under different T_w conditions are summarized in Table S1 in the Supporting Information.

These crystal growth behaviors can be explained by the Burton-Cabrera-Frank (BCF) theory of crystal growth.⁵⁹⁻⁶⁰ The crystal growth process is controlled by the supersaturation (σ) of local growth environment, which is defined as $\sigma = \ln(c/c_0)$, where c and c_0 are the local concentration of gas precursor and equilibrium concentration of gas precursor, respectively. In the vapor phase growth of MX_2 , low supersaturation promotes screw dislocation-driven growth mode, which results in spiral nanoplates, whereas high supersaturation leads to layer-by-layer growth mode characterized by monolayers as well as few layer nanoplates.^{40, 45, 61} Here in our experiments, the local concentration c is influenced by three factors: the equilibria of the reactions between WS_2 precursor and water vapor at 1200°C that control the generation of gas precursors; the transport and distribution of gaseous species along the tube reactor; as well as the consumption of gas precursor during the deposition before reaching a particular growth region. Although the latter two factors are hard to predict and control, we can actively control the generation of gas precursors by tuning the amount of water vapor: higher vapor pressure of water in the reactor leads to higher local concentration c for WS_2 growth. On the other hand, the equilibrium concentration c_0 is

determined by the thermodynamic equilibrium of the WS₂ deposition reaction, which is only affected by the local temperature. If local concentration c is fixed, as temperature decreases along the tube reactor, the equilibrium concentration c_0 also decreases, which results in increasing supersaturation. Therefore, on the upstream side of the substrate where the local concentration c has not been consumed much, the supersaturation increases along the substrate; however, when the gas precursors are progressively consumed downstream, the supersaturation would decrease. This variation of supersaturation leads to the observed spatial distributions of various WS₂ morphologies along the substrate (Figure 2b) at a particular water vapor release rate.

Furthermore, the ability to control supersaturation also enables the controlled edge epitaxial growth of lateral MX₂ heterostructures. The key is to control the delivery of water vapor properly for each MX₂ material. We successfully grew large-area WS₂-MoS₂ heterostructures by switching the MX₂ source during the growth. As shown in Figure 3a, while WS₂ was reacting at 1200 °C in Zone 2, a second precursor boat containing MoS₂ placed upstream would stay cool and unreactive in Zone 1, where the temperature is around 500 °C during the reaction (Figure S5). After the WS₂ growth is completed, the MoS₂ precursor was pushed into Zone 2 as the WS₂ precursor was pushed out of Zone 2 using magnet coupled positioner and quartz rods. This allowed the *in situ* switch from WS₂ growth to MoS₂ growth without exposure to ambient conditions. One key to the success of lateral heterostructure growth is that the water source temperature T_w needs to be lowered to ~85 °C, which leads to a low supersaturation of MoS₂ that only allows the MoS₂ growth seeded around the edges of the existing WS₂ layers via lateral epitaxy instead of self-nucleation. With this lateral epitaxy, three common types of heterostructures can be achieved as determined by the morphology of the WS₂ products in the first step, as illustrated in Figure 3b-d: lateral epitaxy on WS₂ monolayers would produce typical lateral heterostructures of monolayers (Figure 3b),

however, lateral epitaxy on few layers could result in two types of structures, depending on the morphology of the multilayer WS_2 in the first step. In Type A where the layers of WS_2 have different sizes, lateral epitaxy would result in both lateral heterostructure and vertical heterostructure at different regions (Figure 3c); in Type B both layers have the same size and shape (Figure 3d), so only few layer lateral heterostructures would be produced. Because the starting few layer WS_2 plates are often found together, Type A and B are usually produced together on the substrate in high density (as shown in low magnification optical images in Figure S6).

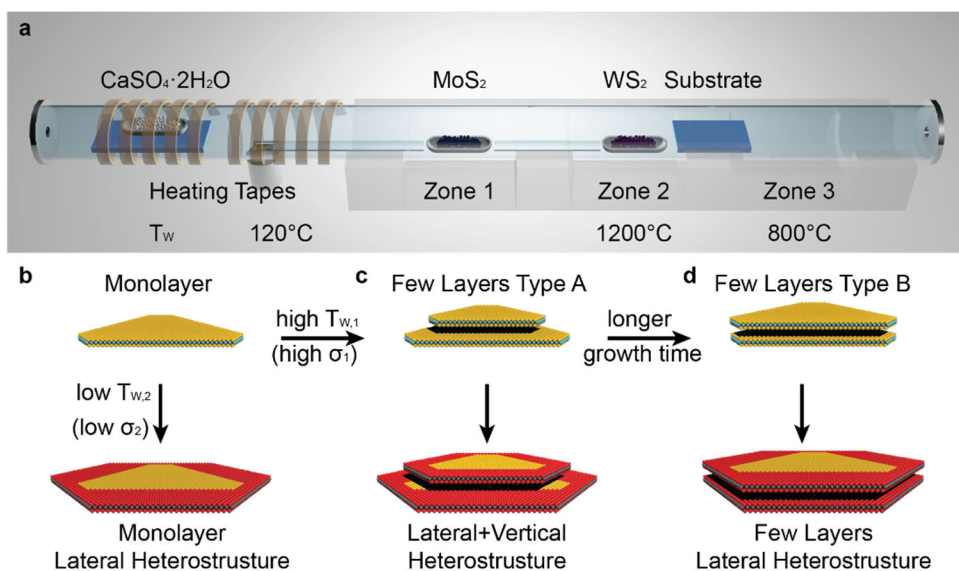


Figure 3. (a) Schematic illustration of the experimental setup for WS_2 - MoS_2 heterostructure growth by water-assisted chemical vapor transport. The MoS_2 precursor was placed upstream of WS_2 precursor. When MoS_2 precursor was pushed into Zone 2, WS_2 precursor would simultaneously be pushed into Zone 3, which is downstream of the substrate. (b-d) The growth pathways of WS_2 and WS_2 - MoS_2 heterostructures via lateral epitaxy leading to three common types of heterostructures.

We characterized these representative heterostructures using spatially resolved Raman and PL spectroscopy (Figure 4). These are large area heterostructures with lateral dimension greater than 100 μm . Figure 4a shows the optical microscope image of a monolayer WS_2 - MoS_2 lateral heterostructure, where an optical contrast can be directly observed. The brighter region corresponds to the WS_2 grown in the first step, and the darker region corresponds to the MoS_2 grown in the second step. The PL spectra in Figure 4f (excited by 532 nm laser) show a strong peak at around 640 nm (1.94 eV) for WS_2 and 672 nm (1.84 eV) for MoS_2 , which are consistent with previous reports.³⁵ The corresponding integrated PL intensity composite map of monolayer heterostructures in Figure 4c shows good agreement with the optical contrast. Interestingly, spatial inhomogeneity was observed within each region. Three-fold “radioactive symbol” like pattern was observed in the WS_2 region, whereas the edges of MoS_2 region are significantly brighter, especially at the corners. In the corresponding Raman mapping (Figure 4b), where WS_2 was mapped by 2LA peak (531 cm^{-1}) and MoS_2 by A_{1g} peak (406 cm^{-1}), the pattern in WS_2 region remained the same, but no obvious pattern was seen in MoS_2 region, suggesting different origins of inhomogeneity. The three-fold “radioactive symbol” like patterns are often observed in CVD synthesized WS_2 , which was attributed to the spatial distribution of different types and densities of point defects.⁶²⁻⁶⁵ The enhanced PL on the edge of MoS_2 might be related to the oxygen binding to defects on the edge after the sample is exposed to ambient environment.⁶⁶⁻⁶⁹ Note the boundaries between WS_2 and MoS_2 also showed brighter response in both PL and Raman. This could be related to potential charge transfer at the heterojunction of monolayer WS_2 and MoS_2 ,⁷⁰ which needs to be further investigated.

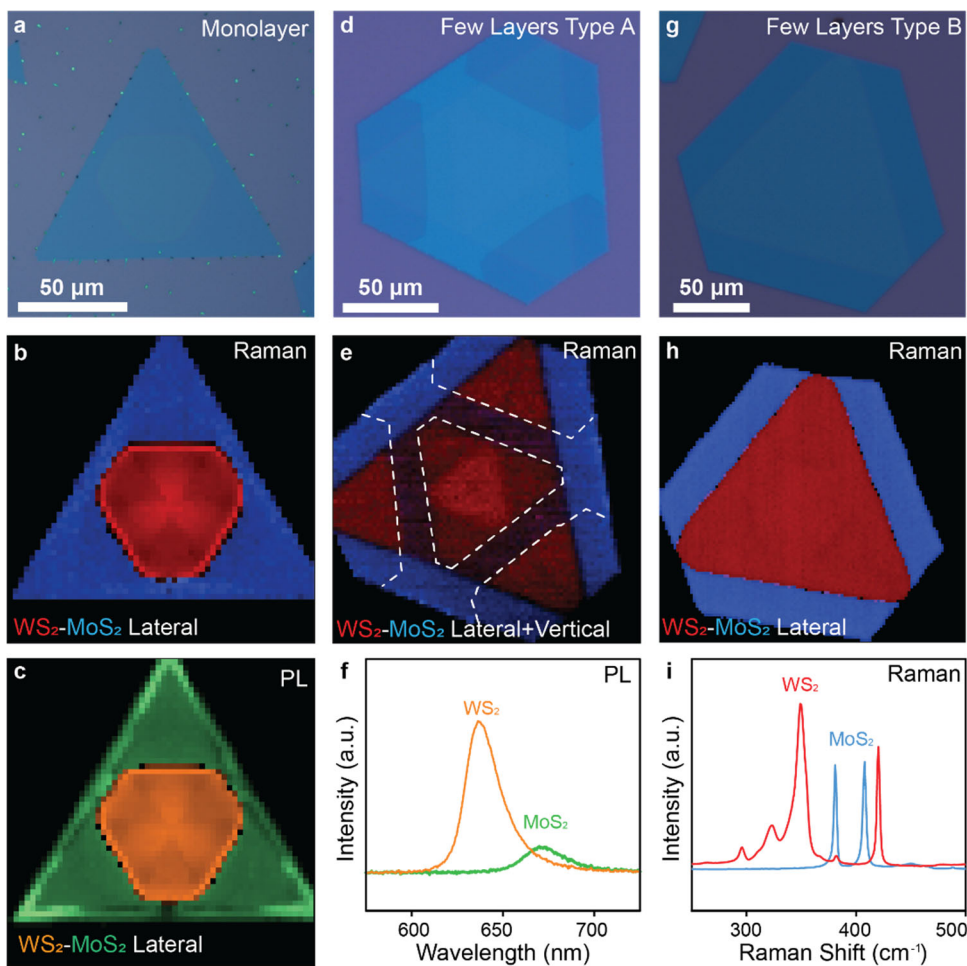


Figure 4. Optical image (a), Raman (b) and PL (c) mapping of a representative monolayer WS₂-MoS₂ heterostructure. Optical image (d) and Raman mapping (e) of a representative few layer type A WS₂-MoS₂ heterostructures. (f) PL Spectrum of the monolayer WS₂-MoS₂ heterostructure. Optical image (g) and Raman mapping (h) of a representative few layer type B WS₂-MoS₂ heterostructure. (i) Raman Spectrum of the few layer WS₂ -MoS₂ heterostructure. The samples were excited by 532 nm laser.

Raman mappings on the representative few layers type A and type B heterostructures were also performed. The particular type A heterostructures in Figure 4e was mapped by using 422 nm laser

excitation instead of 532 nm, since 532 nm laser would enhance the Raman intensity of WS₂ via a double-resonant process⁷¹ that buries the Raman signature of MoS₂ in the overlapped region. Non-resonant 442 nm laser would bring the peaks close to about equivalent intensity, thus helping to distinguish peaks from each material. The particular nanoplate in Figure 4b and 4e consists of a 3-layer base, which was confirmed by AFM as shown in Figure S7. In addition to that, another layer of smaller size WS₂ was grown during the first growth step. After the lateral epitaxial growth of MoS₂ in the second step, part of the extended MoS₂ region on the top layer overlaps with the WS₂ beneath, resulting in vertical heterostructures of WS₂-MoS₂. The overlapped region, as outlined by the dashed lines in Figure 4e, showed depressed Raman signals from both WS₂ and MoS₂ in comparison to the homostructure near it. The particular type B heterostructure in Figure 4g and 4h also consists of 3 layers of WS₂ and MoS₂, which was confirmed by AFM as shown in Figure S7. This few layer WS₂-MoS₂ lateral heterostructure showed the same difference in optical contrast seen in monolayer heterostructures, however the three-fold “radioactive symbol” is much less obvious. These Raman mapping results confirmed the various growth pathways and the type of MX₂ heterostructures that can be formed with water-assisted CVD (Figure 3).

In summary, we have demonstrated controllable synthesis of various WS₂ nanostructures and WS₂-MoS₂ heterostructures using water-assisted chemical vapor transport. By utilizing the thermal decomposition of CaSO₄·2H₂O, we developed a simple method to precisely control the amount of water vapor in a CVD reactor. This method can not only provide the ability to generate water vapor with a wider range than using liquid water source, but also can be easily integrated into a CVD reaction setup. Controlled amount of water vapor, and thus controlled supersaturation of the CVD reactions, enabled us to achieve controllable growth of various WS₂ monolayer, few-layer and spiral nanoplates on SiO₂/Si substrates, the lateral epitaxial growth of MoS₂ layer on the

edge of WS₂, and more reproducible growth of different types of large area heterostructures of WS₂-MoS₂. PL and Raman mappings confirmed three different types of heterostructures. This research provides a facile and effective approach to control the water vapor in vapor phase growth of MX₂ materials and reveal new insights into the growth mechanisms of MX₂, and thus leads to a general approach to the controllable growth of other metal chalcogenides and their heterostructures.

ASSOCIATED CONTENT

Supporting Information.

Experimental sections; the representative optical images of MX₂ grown at different conditions; examples of the temperature profiles of the reactor system; powder X-ray diffraction of the WS₂ and MoS₂ precursors after reaction; summary of the morphology distribution for WS₂ growth at different T_w; optical images of WS₂ and WS₂-MoS₂ heterostructures. atomic force microscopy images WS₂-MoS₂ heterostructures.

AUTHOR INFORMATION

Corresponding Author

*Correspondence should be addressed to S.J. (jin@chem.wisc.edu).

Notes

The authors declare no competing financial interest.

ACKNOWLEDGMENT

This research is supported by the Department of Energy, Office of Basic Energy Sciences, Division of Materials Science and Engineering, under Award DE-FG02-09ER46664

REFERENCES

- (1) Zeng, M.; Xiao, Y.; Liu, J.; Yang, K.; Fu, L. Exploring Two-Dimensional Materials toward the Next-Generation Circuits: From Monomer Design to Assembly Control *Chem. Rev.* **2018**, *118*, 6236.
- (2) Novoselov, K. S.; Mishchenko, A.; Carvalho, A.; Castro Neto, A. H. 2D materials and van der Waals heterostructures *Science* **2016**, *353*, aac9439.
- (3) Zhou, J.; Lin, J.; Huang, X.; Zhou, Y.; Chen, Y.; Xia, J.; Wang, H.; Xie, Y.; Yu, H.; Lei, J., *et al.* A library of atomically thin metal chalcogenides *Nature* **2018**, *556*, 355.
- (4) Briggs, N.; Subramanian, S.; Lin, Z.; Li, X. F.; Zhang, X. T.; Zhang, K. H.; Xiao, K.; Geohagan, D.; Wallace, R.; Chen, L. Q., *et al.* A roadmap for electronic grade 2D materials *2D Mater.* **2019**, *6*, 022001.
- (5) Ma, Y.; Ajayan, P. M.; Yang, S.; Gong, Y. Recent Advances in Synthesis and Applications of 2D Junctions *Small* **2018**, *14*, 1801606.
- (6) Liu, B.; Abbas, A.; Zhou, C. Two-Dimensional Semiconductors: From Materials Preparation to Electronic Applications *Adv. Electron. Mater.* **2017**, *3*, 1700045.
- (7) Liu, Y.; Weiss, N. O.; Duan, X.; Cheng, H.-C.; Huang, Y.; Duan, X. Van der Waals heterostructures and devices *Nat. Rev. Mater.* **2016**, *1*, 16042.
- (8) Wang, Q. H.; Kalantar-Zadeh, K.; Kis, A.; Coleman, J. N.; Strano, M. S. Electronics and optoelectronics of two-dimensional transition metal dichalcogenides *Nat. Nanotechnol.* **2012**, *7*, 699.
- (9) Radisavljevic, B.; Radenovic, A.; Brivio, J.; Giacometti, V.; Kis, A. Single-layer MoS₂ transistors *Nat. Nanotechnol.* **2011**, *6*, 147.
- (10) Mak, K. F.; Lee, C.; Hone, J.; Shan, J.; Heinz, T. F. Atomically thin MoS₂: a new direct-gap semiconductor *Phys. Rev. Lett.* **2010**, *105*, 136805.
- (11) Novoselov, K. S.; Jiang, D.; Schedin, F.; Booth, T. J.; Khotkevich, V. V.; Morozov, S. V.; Geim, A. K. Two-dimensional atomic crystals *Proc. Natl. Acad. Sci. U.S.A.* **2005**, *102*, 10451.
- (12) Nicolosi, V.; Chhowalla, M.; Kanatzidis, M. G.; Strano, M. S.; Coleman, J. N. Liquid Exfoliation of Layered Materials *Science* **2013**, *340*, 1226419.
- (13) Coleman, J. N.; Lotya, M.; O'Neill, A.; Bergin, S. D.; King, P. J.; Khan, U.; Young, K.; Gaucher, A.; De, S.; Smith, R. J., *et al.* Two-Dimensional Nanosheets Produced by Liquid Exfoliation of Layered Materials *Science* **2011**, *331*, 568.
- (14) Manzeli, S.; Ovchinnikov, D.; Pasquier, D.; Yazyev, O. V.; Kis, A. 2D transition metal dichalcogenides *Nat. Rev. Mater.* **2017**, *2*, 17033.
- (15) Chen, P.; Zhang, Z.; Duan, X.; Duan, X. Chemical synthesis of two-dimensional atomic crystals, heterostructures and superlattices *Chem. Soc. Rev.* **2018**, *47*, 3129.
- (16) Chen, J.; Zhao, X.; Tan, S. J. R.; Xu, H.; Wu, B.; Liu, B.; Fu, D.; Fu, W.; Geng, D.; Liu, Y., *et al.* Chemical Vapor Deposition of Large-Size Monolayer MoSe₂ Crystals on Molten Glass *J. Am. Chem. Soc.* **2017**, *139*, 1073.

- (17) Gong, Y.; Ye, G.; Lei, S.; Shi, G.; He, Y.; Lin, J.; Zhang, X.; Vajtai, R.; Pantelides, S. T.; Zhou, W., *et al.* Synthesis of Millimeter-Scale Transition Metal Dichalcogenides Single Crystals *Adv. Funct. Mater.* **2016**, *26*, 2009.
- (18) Huang, J.-K.; Pu, J.; Hsu, C.-L.; Chiu, M.-H.; Juang, Z.-Y.; Chang, Y.-H.; Chang, W.-H.; Iwasa, Y.; Takenobu, T.; Li, L.-J. Large-Area Synthesis of Highly Crystalline WSe₂ Monolayers and Device Applications *ACS Nano* **2014**, *8*, 923.
- (19) Li, M.-Y.; Shi, Y.; Cheng, C.-C.; Lu, L.-S.; Lin, Y.-C.; Tang, H.-L.; Tsai, M.-L.; Chu, C.-W.; Wei, K.-H.; He, J.-H., *et al.* Epitaxial growth of a monolayer WSe₂-MoS₂ lateral p-n junction with an atomically sharp interface *Science* **2015**, *349*, 524.
- (20) Duan, X.; Wang, C.; Shaw, J. C.; Cheng, R.; Chen, Y.; Li, H.; Wu, X.; Tang, Y.; Zhang, Q.; Pan, A., *et al.* Lateral epitaxial growth of two-dimensional layered semiconductor heterojunctions *Nat. Nanotechnol.* **2014**, *9*, 1024.
- (21) Gong, Y.; Lei, S.; Ye, G.; Li, B.; He, Y.; Keyshar, K.; Zhang, X.; Wang, Q.; Lou, J.; Liu, Z., *et al.* Two-Step Growth of Two-Dimensional WSe₂/MoSe₂ Heterostructures *Nano. Lett.* **2015**, *15*, 6135.
- (22) Gong, Y.; Lin, J.; Wang, X.; Shi, G.; Lei, S.; Lin, Z.; Zou, X.; Ye, G.; Vajtai, R.; Yakobson, B. I., *et al.* Vertical and in-plane heterostructures from WS₂/MoS₂ monolayers *Nat. Mater.* **2014**, *13*, 1135.
- (23) Gong, Y.; Lin, Z.; Ye, G.; Shi, G.; Feng, S.; Lei, Y.; Elías, A. L.; Perea-Lopez, N.; Vajtai, R.; Terrones, H., *et al.* Tellurium-Assisted Low-Temperature Synthesis of MoS₂ and WS₂ Monolayers *ACS Nano* **2015**, *9*, 11658.
- (24) Lin, Y.-C.; Zhang, W.; Huang, J.-K.; Liu, K.-K.; Lee, Y.-H.; Liang, C.-T.; Chu, C.-W.; Li, L.-J. Wafer-scale MoS₂ thin layers prepared by MoO₃ sulfurization *Nanoscale* **2012**, *4*, 6637.
- (25) Najmaei, S.; Liu, Z.; Zhou, W.; Zou, X.; Shi, G.; Lei, S.; Yakobson, B. I.; Idrobo, J.-C.; Ajayan, P. M.; Lou, J. Vapour phase growth and grain boundary structure of molybdenum disulphide atomic layers *Nat. Mater.* **2013**, *12*, 754.
- (26) Wang, X.; Gong, Y.; Shi, G.; Chow, W. L.; Keyshar, K.; Ye, G.; Vajtai, R.; Lou, J.; Liu, Z.; Ringe, E., *et al.* Chemical Vapor Deposition Growth of Crystalline Monolayer MoSe₂ *ACS Nano* **2014**, *8*, 5125.
- (27) Zhou, J.; Tang, B.; Lin, J.; Lv, D.; Shi, J.; Sun, L.; Zeng, Q.; Niu, L.; Liu, F.; Wang, X., *et al.* Morphology Engineering in Monolayer MoS₂-WS₂ Lateral Heterostructures *Adv. Funct. Mater.* **2018**, *28*, 1801568.
- (28) Samad, L.; Bladow, S. M.; Ding, Q.; Zhuo, J.; Jacobberger, R. M.; Arnold, M. S.; Jin, S. Layer-Controlled Chemical Vapor Deposition Growth of MoS₂ Vertical Heterostructures via van der Waals Epitaxy *ACS Nano* **2016**, *10*, 7039.
- (29) Zhang, X.; Meng, F.; Christianson, J. R.; Arroyo-Torres, C.; Lukowski, M. A.; Liang, D.; Schmidt, J. R.; Jin, S. Vertical Heterostructures of Layered Metal Chalcogenides by van der Waals Epitaxy *Nano. Lett.* **2014**, *14*, 3047.
- (30) Yu, Y.; Li, C.; Liu, Y.; Su, L.; Zhang, Y.; Cao, L. Controlled Scalable Synthesis of Uniform, High-Quality Monolayer and Few-layer MoS₂ Films *Sci. Rep.* **2013**, *3*, 1866.
- (31) Xie, S.; Tu, L.; Han, Y.; Huang, L.; Kang, K.; Lao, K. U.; Poddar, P.; Park, C.; Muller, D. A.; DiStasio, R. A., *et al.* Coherent, atomically thin transition-metal dichalcogenide superlattices with engineered strain *Science* **2018**, *359*, 1131.
- (32) Eichfeld, S. M.; Colon, V. O.; Nie, Y.; Cho, K.; Robinson, J. A. Controlling nucleation of monolayer WSe₂ during metal-organic chemical vapor deposition growth *2D Mater.* **2016**, *3*, 025015.

- (33) Kang, K.; Xie, S.; Huang, L.; Han, Y.; Huang, P. Y.; Mak, K. F.; Kim, C.-J.; Muller, D.; Park, J. High-mobility three-atom-thick semiconducting films with wafer-scale homogeneity *Nature* **2015**, *520*, 656.
- (34) Lin, Y.-C.; Jariwala, B.; Bersch, B. M.; Xu, K.; Nie, Y.; Wang, B.; Eichfeld, S. M.; Zhang, X.; Choudhury, T. H.; Pan, Y., *et al.* Realizing Large-Scale, Electronic-Grade Two-Dimensional Semiconductors *ACS Nano* **2018**, *12*, 965.
- (35) Sahoo, P. K.; Memaran, S.; Xin, Y.; Balicas, L.; Gutierrez, H. R. One-pot growth of two-dimensional lateral heterostructures via sequential edge-epitaxy *Nature* **2018**, *553*, 63.
- (36) Zhang, Z.; Chen, P.; Duan, X.; Zang, K.; Luo, J.; Duan, X. Robust epitaxial growth of two-dimensional heterostructures, multiheterostructures, and superlattices *Science* **2017**, *357*, 788.
- (37) Zheng, B.; Ma, C.; Li, D.; Lan, J.; Zhang, Z.; Sun, X.; Zheng, W.; Yang, T.; Zhu, C.; Ouyang, G., *et al.* Band Alignment Engineering in Two-Dimensional Lateral Heterostructures *J. Am. Chem. Soc.* **2018**, *140*, 11193.
- (38) Duan, X.; Wang, C.; Fan, Z.; Hao, G.; Kou, L.; Halim, U.; Li, H.; Wu, X.; Wang, Y.; Jiang, J., *et al.* Synthesis of $WS_{2x}Se_{2-2x}$ Alloy Nanosheets with Composition-Tunable Electronic Properties *Nano. Lett.* **2016**, *16*, 264.
- (39) Fan, X.; Jiang, Y.; Zhuang, X.; Liu, H.; Xu, T.; Zheng, W.; Fan, P.; Li, H.; Wu, X.; Zhu, X., *et al.* Broken Symmetry Induced Strong Nonlinear Optical Effects in Spiral WS_2 Nanosheets *ACS Nano* **2017**, *11*, 4892.
- (40) Fan, X.; Zhao, Y.; Zheng, W.; Li, H.; Wu, X.; Hu, X.; Zhang, X.; Zhu, X.; Zhang, Q.; Wang, X., *et al.* Controllable Growth and Formation Mechanisms of Dislocated WS_2 Spirals *Nano. Lett.* **2018**, *18*, 3885.
- (41) Huang, C.; Wu, S.; Sanchez, A. M.; Peters, J. J. P.; Beanland, R.; Ross, J. S.; Rivera, P.; Yao, W.; Cobden, D. H.; Xu, X. Lateral heterojunctions within monolayer $MoSe_2$ - WSe_2 semiconductors *Nat. Mater.* **2014**, *13*, 1096.
- (42) Cai, Z.; Liu, B.; Zou, X.; Cheng, H.-M. Chemical Vapor Deposition Growth and Applications of Two-Dimensional Materials and Their Heterostructures *Chem. Rev.* **2018**, *118*, 6091.
- (43) Liu, K.-K.; Zhang, W.; Lee, Y.-H.; Lin, Y.-C.; Chang, M.-T.; Su, C.-Y.; Chang, C.-S.; Li, H.; Shi, Y.; Zhang, H., *et al.* Growth of Large-Area and Highly Crystalline MoS_2 Thin Layers on Insulating Substrates *Nano. Lett.* **2012**, *12*, 1538.
- (44) Zhang, J.; Yu, H.; Chen, W.; Tian, X.; Liu, D.; Cheng, M.; Xie, G.; Yang, W.; Yang, R.; Bai, X., *et al.* Scalable Growth of High-Quality Polycrystalline MoS_2 Monolayers on SiO_2 with Tunable Grain Sizes *ACS Nano* **2014**, *8*, 6024.
- (45) Shearer, M. J.; Samad, L.; Zhang, Y.; Zhao, Y.; Poretzky, A.; Eliceiri, K. W.; Wright, J. C.; Hamers, R. J.; Jin, S. Complex and Noncentrosymmetric Stacking of Layered Metal Dichalcogenide Materials Created by Screw Dislocations *J. Am. Chem. Soc.* **2017**, *139*, 3496.
- (46) Zhang, L.; Liu, K.; Wong, A. B.; Kim, J.; Hong, X.; Liu, C.; Cao, T.; Louie, S. G.; Wang, F.; Yang, P. Three-Dimensional Spirals of Atomic Layered MoS_2 *Nano. Lett.* **2014**, *14*, 6418.
- (47) Ly, T. H.; Zhao, J.; Kim, H.; Han, G. H.; Nam, H.; Lee, Y. H. Vertically Conductive MoS_2 Spiral Pyramid *Adv. Mater.* **2016**, *28*, 7723.
- (48) Chen, L.; Liu, B.; Abbas, A. N.; Ma, Y.; Fang, X.; Liu, Y.; Zhou, C. Screw-Dislocation-Driven Growth of Two-Dimensional Few-Layer and Pyramid-like WSe_2 by Sulfur-Assisted Chemical Vapor Deposition *ACS Nano* **2014**, *8*, 11543.
- (49) Kastl, C.; Chen, C. T.; Kuykendall, T.; Shevitski, B.; Darlington, T. P.; Borys, N. J.; Krayev, A.; Schuck, P. J.; Aloni, S.; Schwartzberg, A. M. The important role of water in growth of monolayer transition metal dichalcogenides *2D Mater.* **2017**, *4*, 021024.

- (50) Hata, K.; Futaba, D. N.; Mizuno, K.; Namai, T.; Yumura, M.; Iijima, S. Water-Assisted Highly Efficient Synthesis of Impurity-Free Single-Walled Carbon Nanotubes *Science* **2004**, *306*, 1362.
- (51) Amama, P. B.; Pint, C. L.; McJilton, L.; Kim, S. M.; Stach, E. A.; Murray, P. T.; Hauge, R. H.; Maruyama, B. Role of Water in Super Growth of Single-Walled Carbon Nanotube Carpets *Nano. Lett.* **2009**, *9*, 44.
- (52) Zhou, W.; Zhan, S.; Ding, L.; Liu, J. General Rules for Selective Growth of Enriched Semiconducting Single Walled Carbon Nanotubes with Water Vapor as in Situ Etchant *J. Am. Chem. Soc.* **2012**, *134*, 14019.
- (53) Asif, M.; Tan, Y.; Pan, L.; Li, J.; Rashad, M.; Usman, M. Thickness Controlled Water Vapors Assisted Growth of Multilayer Graphene by Ambient Pressure Chemical Vapor Deposition *J. Phys. Chem. C* **2015**, *119*, 3079.
- (54) Wang, L.; Wu, B.; Liu, H.; Huang, L.; Li, Y.; Guo, W.; Chen, X.; Peng, P.; Fu, L.; Yang, Y., *et al.* Water-assisted growth of large-sized single crystal hexagonal boron nitride grains *Mater. Chem. Front.* **2017**, *1*, 1836.
- (55) Moh, G. H. High-temperature metal sulfide chemistry *Top. Curr. Chem.* **1978**, *76*, 107.
- (56) Brainard, W. A. The thermal stability and friction of the disulfides, diselenides, and ditellurides of molybdenum and tungsten in vacuum (10^{-9} to 10^{-6} torr) *NASA Technical Note* **1969**, *TN D-5141*, 1.
- (57) Dong, J.; Zhang, L.; Ding, F. Kinetics of Graphene and 2D Materials Growth *Adv. Mater.* **0**, 1801583.
- (58) Wang, S.; Rong, Y.; Fan, Y.; Pacios, M.; Bhaskaran, H.; He, K.; Warner, J. H. Shape Evolution of Monolayer MoS₂ Crystals Grown by Chemical Vapor Deposition *Chem. Mater.* **2014**, *26*, 6371.
- (59) Burton, W. K.; Cabrera, N.; Frank, F. C. The Growth of Crystals and the Equilibrium Structure of Their Surfaces *Philos. Trans. R. Soc. Lond. A* **1951**, *243*, 299.
- (60) Woodruff, D. P. How does your crystal grow? A commentary on Burton, Cabrera and Frank (1951) 'The growth of crystals and the equilibrium structure of their surfaces' *Philos. Trans. R. Soc. A* **2015**, *373*, 20140230.
- (61) Meng, F.; Morin, S. A.; Forticaux, A.; Jin, S. Screw Dislocation Driven Growth of Nanomaterials *Acc. Chem. Res.* **2013**, *46*, 1616.
- (62) Lin, Y.-C.; Li, S.; Komsa, H.-P.; Chang, L.-J.; Krasheninnikov, A. V.; Eda, G.; Suenaga, K. Revealing the Atomic Defects of WS₂ Governing Its Distinct Optical Emissions *Adv. Funct. Mater.* **2018**, *28*, 1704210.
- (63) Sheng, Y.; Wang, X.; Fujisawa, K.; Ying, S.; Elias, A. L.; Lin, Z.; Xu, W.; Zhou, Y.; Korsunsky, A. M.; Bhaskaran, H., *et al.* Photoluminescence Segmentation within Individual Hexagonal Monolayer Tungsten Disulfide Domains Grown by Chemical Vapor Deposition *ACS Appl. Mater. Interfaces* **2017**, *9*, 15005.
- (64) Liu, H.; Lu, J.; Ho, K.; Hu, Z.; Dang, Z.; Carvalho, A.; Tan, H. R.; Tok, E. S.; Sow, C. H. Fluorescence Concentric Triangles: A Case of Chemical Heterogeneity in WS₂ Atomic Monolayer *Nano. Lett.* **2016**, *16*, 5559.
- (65) Rosenberger, M. R.; Chuang, H.-J.; McCreary, K. M.; Li, C. H.; Jonker, B. T. Electrical Characterization of Discrete Defects and Impact of Defect Density on Photoluminescence in Monolayer WS₂ *ACS Nano* **2018**, *12*, 1793.

- (66) Gogoi, P. K.; Hu, Z.; Wang, Q.; Carvalho, A.; Schmidt, D.; Yin, X.; Chang, Y.-H.; Li, L.-J.; Sow, C. H.; Neto, A. H. C., *et al.* Oxygen Passivation Mediated Tunability of Trion and Excitons in MoS₂ *Phys. Rev. Lett.* **2017**, *119*, 077402.
- (67) Gutiérrez, H. R.; Perea-López, N.; Elías, A. L.; Berkdemir, A.; Wang, B.; Lv, R.; López-Urías, F.; Crespi, V. H.; Terrones, H.; Terrones, M. Extraordinary Room-Temperature Photoluminescence in Triangular WS₂ Monolayers *Nano. Lett.* **2013**, *13*, 3447.
- (68) Kotsakidis, J. C.; Zhang, Q.; Vazquez de Parga, A. L.; Currie, M.; Helmerson, K.; Gaskill, D. K.; Fuhrer, M. S. Oxidation of Monolayer WS₂ in Ambient Is a Photoinduced Process *Nano. Lett.* **2019**, *19*, 5205.
- (69) Hu, Z.; Avila, J.; Wang, X.; Leong, J. F.; Zhang, Q.; Liu, Y.; Asensio, M. C.; Lu, J.; Carvalho, A.; Sow, C. H., *et al.* The Role of Oxygen Atoms on Excitons at the Edges of Monolayer WS₂ *Nano. Lett.* **2019**, *19*, 4641.
- (70) Shearer, M. J.; Li, M.-Y.; Li, L.-J.; Jin, S.; Hamers, R. J. Nanoscale Surface Photovoltage Mapping of 2D Materials and Heterostructures by Illuminated Kelvin Probe Force Microscopy *J. Phys. Chem. C* **2018**, *122*, 13564.
- (71) Berkdemir, A.; Gutierrez, H. R.; Botello-Mendez, A. R.; Perea-Lopez, N.; Elias, A. L.; Chia, C. I.; Wang, B.; Crespi, V. H.; Lopez-Urias, F.; Charlier, J. C., *et al.* Identification of individual and few layers of WS₂ using Raman Spectroscopy *Sci. Rep.* **2013**, *3*, 1755.

TOC Graphic:

